Elastic scattering in the math xmlns="http://www.w3.org/1998/Math/MathML">mrow>mmultiscripts>mi mathvariant="normal">N/mi>mprescripts>/mprescripts>none>/none>mn>12/mn>/mmultiscripts>mo>+/mo>mmultiscripts>mi>Au/mi>mprescripts>/mprescripts>none>/none>mn>197/mn>/mmultiscripts>/mrow>/math> system at math xmlns="http://www.w3.org/1998/Math/MathML">mrow>msub>mi>E/mi>mtext>lab/mtext>/msub>mo>=/mo>mn>70/mn>/mrow>/math> MeV

P. L. D. Magro, V. Guimarães, R. Linares, J. Rangel, J. C. Zamora, G. V. Rogachev, E. Koshchiy, J. Bishop, M. Barbui, C. E. Parker, B. Roeder, and A. Saastomoinen

Phys. Rev. C **111**, 034609 — Published 11 March 2025

DOI: 10.1103/PhysRevC.111.034609

Elastic scattering in the ^{12}N + ^{197}Au system at E_{lab} = 70 MeV.

P. L. D. Magro,[1] V. Guimarães,[1] R. Linares,[2] J. Rangel,[3]
J. C. Zamora,[4] G. V. Rogachev,[5,6,7] E. Koshchiy,[6] J. Bishop,[6,8]
M. Barbui,[6] C. E. Parker,[6] B. Roeder,[6] and A. Saastomoinen[6]

[1]*Instituto de Física, Universidade de São Paulo, São Paulo, 05508-090, São Paulo, Brazil*

[2]*Instituto de Física, Universidade Federal Fluminense, 24210-340 Niterói, Rio de Janeiro, Brazil*

[3]*Departamento de Matemática, Física e Computação, Universidade do Estado do Rio de Janeiro, Faculdade de Tecnologia, 27537-000 Resende, Rio de Janeiro, Brazil*

[4]*Facility for Rare Isotope Beams, Michigan State University, 48824 East Lansing, Michigan, USA*

[5]*Department of Physics and Astronomy, Texas A&M University, 77843, Texas, USA*

[6]*Cyclotron Institute, Texas A&M University, 77843, Texas, USA*

[7]*Nuclear Solutions Institute, Texas A&M University, 77843, Texas, USA*

[8]*School of Physics and Astronomy, University of Birmingham, B15 2TT, Birmingham, United Kingdom*

(Dated: February 18, 2025)

Abstract

Background: Halo structure is an interesting exotic configuration developed in some light weakly bound nuclei, where a valence particle orbits a nuclear core. Signatures of halo structure can be observed in the angular distributions of the elastic scattering induced by these nuclei at energies around the Coulomb barrier. There are some well-studied reactions with neutron-rich halo nuclei, such as ^{6}He and ^{11}Li. However, the portrait is scarce on the proton-rich side. Recent works confirm the halo structure in the ^{8}B nuclei but still lack more experimental studies for other proton-halo candidates, such as ^{12}N and ^{17}F.

Purpose: In this work we report new experimental data for the elastic scattering of ^{12}N on ^{197}Au target at $E_{\rm lab} = 70$ MeV. The ^{12}N is a proton-rich nucleus with proton separation energy $S_p = 600$ keV, which is higher than the ^{8}B ($S_p = 137$ keV) and almost the same as the ^{17}F ($S_p = 601$ keV).

Methods: Data were obtained at the Cyclotron Institute of Texas A&M University where the ^{12}N radioactive beam was produced by the Momentum Achromatic Recoil Spectrometer. The calculation of the optical model was used to fit the measured angular distribution for the elastic scattering and to obtain the reaction cross section σ_R. We also performed continuum discretized coupled-channel calculations to compare with the experimental data.

Results: The angular distribution of the elastic cross sections exhibits a suppression of the Fresnel peak. From the fitting of the optical model, we obtain the total reaction cross section, $\sigma_R = 1269\pm41$ mb. The agreement between the CDCC calculation and the experimental elastic scattering data is limited and the breakdown does not exhaust the measured σ_R.

Conclusions: The resulting reduced reaction cross section $\sigma_{\rm Red}$ for ^{12}N+^{197}Au is large and comparable to the one obtained for ^{8}B+^{208}Pb system. This suggests a strong decoupling of the valence proton from the core because of the low binding energy and a dynamic polarization effect. More research is required to estimate the contribution of core excitation.

I. INTRODUCTION

Light nuclei away from the valley of stability are characterized by low binding energies that, in some cases, lead to the formation of an extended matter distribution and halo

structure in which the valence particle(s) orbits far around a tightly bound nuclear core [1, 2]. These kinds of nuclei are also promising objects for theoretical developments on nuclear open quantum systems, for which the continuum coupling becomes relevant to describe weakly bound states [3].

Signatures of the halo configurations appear already in the angular distribution of the elastic scatterings at energies close to the Coulomb barrier, where the halo configuration has a stronger influence on the reaction mechanism. The angular distribution for elastic scattering of halo nuclei usually exhibits a damping of the Fresnel (or Coulomb-nuclear interference) peak and a large reaction cross section compared to its stable isotope counterpart. Damping of the Fresnel peak arises from the effect of the breakup channel in the presence of Coulomb and/or nuclear potentials [4, 5].

The halo configuration has been well studied for neutron-rich nuclei, such as ^{6}He, ^{11}Li, and ^{11}Be, whereas for proton-rich halo nuclei experimental data are scarce, mostly due to difficulties in producing reasonably intense beams for measurements [6]. One of the most studied proton-rich halo nuclei is the ^{8}B nucleus. In 2019, Mazzocco et al. reported an enormous reaction cross section for ^{8}B + ^{208}Pb at E_{lab}=50 MeV [7]. Two years later, Sparta et al. published new data for elastic scattering in the ^{8}B+^{64}Zn elastic scattering at an energy approximately 1.5 times the Coulomb barrier [8], where a clear Fresnel peak can still be observed (see Fig. 4 in Ref. [8]). In 2022, Yang et al. published data for the elastic and angular correlation of the breakup fragments in the ^{8}B+^{120}Sn system at two energies around the Coulomb barrier [9]. The elastic angular distribution shows a suppression of the Fresnel peak due to the influence of the continuum states in ^{8}B on the elastic scattering, although it is not as significant as observed in the elastic scattering of neutron halo nuclei. Analysis of the angular correlation between the breakup fragments (^{7}Be and proton) provide strong grounds to support that the break-up proceeds through the short-lived continuum states and that the yield of ^{7}Be is almost exhausted by elastic breakup.

Some recent measurements with proton-rich projectiles on heavy targets at energies around the Coulomb barrier involve the ^{10}C [10] and the ^{17}Ne [11], both on the ^{208}Pb target. Their data exhibit damping of the Fresnel peak, but reaction cross sections are comparable to those for weakly bound nuclei in the same mass region. Other proton-halo candidates, such as ^{12}N and ^{17}F, still need further experimental investigations. In this work, we present new experimental data for the elastic scattering of proton-rich ^{12}N on the ^{197}Au target at

E_{lab} = 70 MeV.

This paper is organized as follows: the experimental setup and data are presented in Sect. II. Section III describes the theoretical approaches and discussions about the results. Conclusions are presented in Sect. IV.

II. EXPERIMENTAL DETAILS

The experiment was carried out at the Cyclotron Institute of Texas A&M University, Texas, USA. The radioactive ^{12}N beam was produced from the ^{3}He(^{10}B,^{12}N)n reaction. A $^{10}B^{3+}$ primary beam was delivered by the K150 Cyclotron accelerator at 107 MeV and impinged on a ^{3}He gas cell at 819 Torr and cryogenically cooled at 77 K. The produced ^{12}N particles were selected by the Momentum Achromatic Recoil Spectrometer (MARS). The intensity of the beam was monitored by a scintillator detector positioned downstream of the MARS beam line. Due to the similarity in magnetic rigidity, the secondary beam was composed of $^{12}N^{7+}$ ($\approx$ 44%) and $^{7}Be^{4+}$ ($\approx$ 56%) ions. The average rate of ^{12}N during the experimental runs was about 10^3 pps. The energies of the ^{12}N and ^{7}Be beams, after the scintillator detector and before hitting the ^{197}Au target, were 73.3 MeV and 42.0 MeV, respectively.

A sketch of the scattering chamber is shown in Fig. 1. A 4.7-mg/cm^2-thick ^{197}Au film was mounted on a target holder set at $\sim$ 30° relative to the secondary beam axis. The energy loss of the ^{12}N through the ^{197}Au target is about 6.5 MeV. Therefore, throughout this work, we assume E_{lab}=70 MeV as the incident energy obtained by averaging the ingoing and outgoing energies of the target.

The detection system consisted of three 500-μm-thick double-sided silicon strip detectors (DSSSD) with front and back sides segmented in 128 strips. These detectors were mounted in a diamond-shaped geometry, about 15.3 cm away from the ^{197}Au target. This configuration allowed coverage of scattering angles from $\approx$ 30° to 140° with some angular overlaps between successive DSSSDs. The angular overlaps between the DSSSDs were useful in the normalization procedure. The data readout is based on General Electronics for Time Projection Chambers [12] used in the Texas Active Target Time Projection Chamber [13]. The energy calibration of the detectors was performed using a mixed alpha source with ^{239}Pu, ^{241}Am and ^{244}Cm nuclides, which was also used to determine solid angles. The alpha source

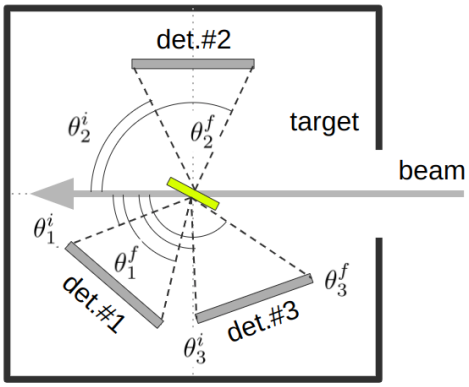

FIG. 1: Sketch of the experimental setup for the measurements of the elastic scattering. The detectors cover the following angles (in the laboratory reference system): $26° < \theta_1 < 81°$ (det.#1), $60° < \theta_2 < 105°$ (det.#2) and $89° < \theta_3 < 140°$ (det.#3).

was placed at the target holder position for the indirect measurement of the solid angles, assuming a uniform emission over the DSSSDs' surface.

Typical energy spectra for two different angular ranges are shown in Fig. 2 (experimental data in blue points). The elastically scattered ^{12}N and ^{7}Be particles are clearly distinguished in the energy spectra at forward angles. The yield of ^{7}Be is very faint at backward angles due to the lower cross section compared to the yield of ^{12}N. The energy resolution, measured as the full width at half maximum (FWHM) of the peak, is about 4.0 MeV, mainly due to the energy spread ($\sim$ 3.0 MeV) related to the acceptance of the MARS, kinematics broadening ($\sim 0.5 - 1.0$ MeV), and energy straggling after the target ($\sim$ 1.0 MeV). The angular resolution is estimated to be about 3° (in the laboratory reference system), based on the size of the beam spot on the target, the relative distances between the target detectors, and the width of the strip of the DSSSD detectors. The yields for the ^{12}N scattering particles were determined from the fit of a Gaussian curve on the peak in the energy spectra, whenever the counting was statistically significant, and by integration of the region for the elastic event, defined according to the energy resolution and centered on the elastic scattering energy. Although the energy resolution does not allow for the distinction of elastic from inelastic scattering, in this work we stick to the term elastic cross section since the inelastic cross section is estimated to be negligible, according to coupled-channel calculations.

Since we do not have a E-ΔE particle identification spectrum, we must rely on simulations to estimate the yields of the ^{11}C breakup fragment in the elastic peak, which could be

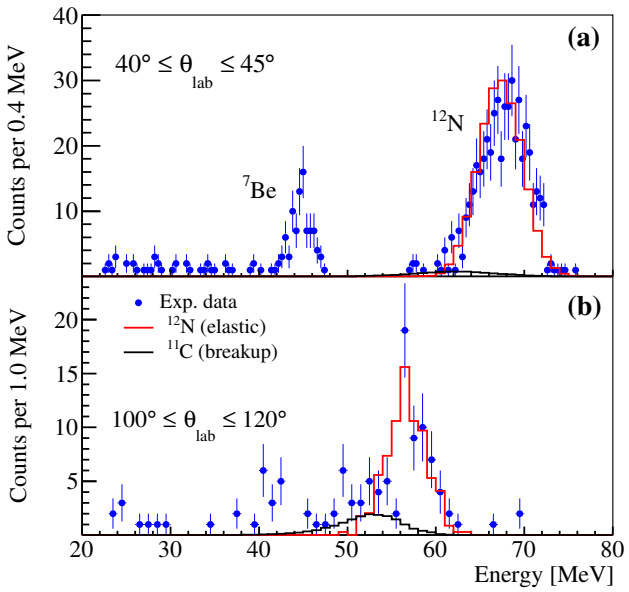

FIG. 2: Energy spectra for ^{12}N + ^{197}Au in the angular ranges of $40° \leq \theta_{\rm lab} \leq 45°$ (panel a) and $100° \leq \theta_{\rm lab} \leq 120°$ (panel b). A small contribution of ^{7}Be (beam contaminant) scattering is observed in the spectra. Simulations of elastic and breakup reaction channels are shown with solid lines.

relevant at very backward angles. Monte Carlo simulations for the elastic and break-up reaction channels were performed using the GEANT4 [14] toolkit, including the relativistic two- and three-body reaction generators [15]. The fitted optical model and the discretized coupled channel continuum cross sections for elastic scattering and elastic breakup (details in Sect. III) were adopted in the simulations. For the break-up channel, the relative energy (in the center-of-mass system) between ^{11}C and p, was assumed to be proportional to the semi-classical photo-dissociation cross section [16]. The results of the simulation are compared with the experimental spectra shown in Fig. 2. The simulated elastically scattered ^{12}N yields are shown as solid red lines and reproduce quite well the experimental data for $40° \leq \theta_{\rm lab} \leq 45°$ (see Fig. 2a). The contribution of ^{11}C from breakup is represented by solid black lines. The ^{11}C breakup fragment becomes important only at backward angles (above 100°, as shown in Fig. 2b) being at most 44% of the total peak for the last data points, between $120° - 130°$. Estimates from the Monte Carlo simulation were employed to correct the measured yields and obtain the elastic cross section.

The experimental angular distribution of the elastic cross section for ^{12}N+^{197}Au at

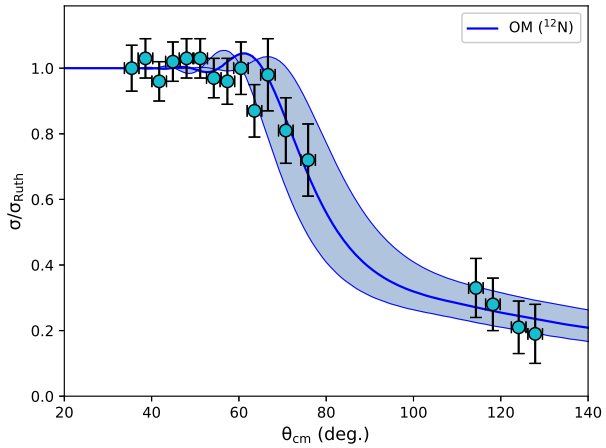

FIG. 3: Elastic scattering angular distribution for the ^{12}N+^{197}Au at E$_{lab}$=70 MeV. Error bars are statistical only. The curve represents the optical model fit to the data. The band curve represents the optical model calculations with energies ranging from 67 to 73 MeV. See text for details.

$E_{\rm lab}$ =70 MeV is shown in Fig. 3, normalized to the Rutherford cross sections. The error bars correspond only to the statistical uncertainty. Other systematic uncertainties (beam axis and target thickness uniformity) account for about 10%. No additional normalization was necessary, which is considered a validation of the indirect solid angle measurement with the alpha source. We also checked the yields of the contaminant ^{7}Be which reproduce well by Rutherford cross section for the ^{7}Be+^{197}Au system at E$_{lab}$=41 MeV. This is considered a good indication of the accuracy and consistency of the data reduction. The missing cross sections in the angular region of $\theta_{c.m.}$=80^o to 110^o correspond to the yields from det. #2 (see Fig. 1). The data from this detector were somehow compromised by some detection inefficiencies, resulting in low yields. Because these unexpected low yields have not been fully understood, we removed them from the angular distribution. However, this was not a total loss since we still have cross sections in two relevant and important regions of the angular distribution, at fresnel peak and very backward angles, allowing analysis and discussion of the elastic scattering for this system. The optical model curve, also shown in the figure, is described in detail in Sect. III. The suppression of the Fresnel peak is observed in the experimental angular distribution, which suggests a strong coupling with continuum states (breakup).

TABLE I: : Parameters of the optical potentials obtained from the fit of the elastic scattering angular distribution for the systems indicated. The r_V and r_W are reduced radii, using the convention $R_i = r_i \times [A_p^{1/3} + A_t^{1/3}]$ and the reduced Coulomb radius r_C=1.06 fm. The a_V and a_W are the diffuseness. We also include the reduced χ^2.

System	E_{lab} (MeV)	V (MeV)	r_V (fm)	a_V (fm)	W (MeV)	r_W (fm)	a_W (fm)	χ^2/N	Ref.
^{8}B+^{208}Pb	50	50.1	1.00	0.13	15.0	0.93	1.85	1.39	[7]
^{10}C+^{208}Pb	67	82.2	1.19	0.12	17.6	1.60	0.14	3.44	[10]
^{12}C+^{208}Pb	64.9	15.1	1.29	0.33	5.37	1.26	0.33	0.89	[17]
^{12}N+^{197}Au	70	39.7	1.10	0.10	36.2	1.82	0.13	0.35	this work
^{14}N+^{197}Au	92	18.3	1.22	0.19	3.1	1.42	0.21	0.10	[18]
^{17}Ne+^{208}Pb	136	63.1	1.30	0.56	31.9	1.26	0.72	0.36	[11]

III. THEORETICAL ANALYSIS

A. Optical model and reaction cross section

Optical model (OM) calculations were performed for the ^{12}N+^{197}Au system using a complex Woods-Saxon (WS) potential, with parameters adjusted to fit the experimental angular distribution. Parameters from the OM analysis for the ^{10}C+^{208}Pb system at E_{lab}=66 MeV [10] were used as initial guessing values. The best values determined from a least square minimization procedure are shown in Table I and the corresponding fit curve is shown in Fig. 3. The band curve also shown in Fig. 3 has been constructed varying the beam energy in the OM calculation within the experimental uncertainty (± 3.0 MeV) with the WS parameters fixed. As can be observed in this figure, the experimental data points lie mostly within the limits of the band curve.

In Table I, we also include the WS parameters of the optical potential adjusted to fit the experimental data for some similar systems available in the literature. For the ^{12}N+^{197}Au system, the imaginary part of the adjusted optical potential exhibits a large reduced radius (r_W = 1.84 fm) compared to other systems compensated by a short diffuseness (a_w = 0.14 fm). For the ^{8}B+^{208}Pb system, the opposite relationship is observed: a large diffuseness and a short reduced radius for the imaginary part. Nevertheless, this shows that far-reaching imaginary potential is required to absorb flux at surface, and consequently to suppress the

cross sections at the grazing angle in both proton-rich systems. For stable systems, namely ^{12}C and ^{14}N, a shallow imaginary potential is sufficient to reproduce experimental data.

B. Reduction method for reaction cross sections

The total reaction cross sections for the ^{12}N+^{197}Au system was determined to be $\sigma_R = 1269 \pm 41$ mb. The uncertainty was estimated as the standard deviation of the σ_R calculated with the OM at different energies, within the energy uncertainty of $\mathrm{E}_{lab} = 70.0 \pm 3.0$ MeV.

A proper comparison of the total reaction cross section from different systems requires a reduction method that removes (or at least reduces) differences arising from the static properties among systems. Usually, conclusions from these reduction methods for reaction cross sections are limited to very similar systems [19]. Here we discuss two reduction methods, as presented in [20, 21]: i) the fusion function method and ii) the simplified traditional method, which addresses this issue.

1. The fusion function method

In the fusion function method [20], the reduced energy (E_{Red}) and the reduced reaction cross section (σ_{Red}) are defined as follows:

$$E_{\mathrm{Red,1}} = \frac{E_{\mathrm{c.m.}} - V_b}{\hbar\omega}; \qquad \sigma_{\mathrm{Red,1}} = \sigma_R \left[\frac{2E_{\mathrm{c.m.}}}{\hbar\omega R_b^2}\right], \tag{1}$$

where R_b, V_b and $\hbar\omega$ are the radius, height, and width of an inverted parabolic shape adjusted to the Coulomb barrier.

The total reaction cross section consists of fusion and other non-elastic direct reactions such as inelastic, transfer, and breakup cross sections. Fusion cross sections (σ_F) can be estimated using the Wong's approximation [22], which describes penetration through a fixed parabolic barrier. In terms of the reduced variables, Wong's equation transforms itself into an equation referred to as the universal fusion function (UFF) [23], which depends only on the reduced energy given by:

$$\sigma_{\mathrm{UFF}} = \ln\left[1 + \exp(2\pi E_{\mathrm{Red}})\right]. \tag{2}$$

Although Wong's approximation is fairly good at energies above V_b, its validity is limited under the Coulomb barrier (it does not work too well for $E_{\mathrm{Red}} < 0$) and especially for light

TABLE II: Reaction cross sections (σ_R) for selected proton-rich projectiles on ^{197}Au and ^{208}Pb. The optical potential (OP) used to define the parameter of the Coulomb barrier is indicated as well the radius (R_b), height (V_b) and width ($\hbar\omega$) of the adjusted parabolic shape for each system. The reduced quantities as obtained from Eq. 1.

system	$E_{\rm c.m.}$ (MeV)	σ_R (mb)	OP	R_b (fm)	V_b (MeV)	$\hbar\omega$ (MeV)	$E_{\rm Red.}$	$\sigma_{\rm Red.}$
^{8}B+^{208}Pb	48.1	1112	SPP	11.2	49.4	4.49	-0.28	19.0
			V_{00}	11.3	48.8	4.33	-0.07	19.8
			Pol.	11.2	47.8	4.30	0.08	19.9
^{10}C+^{208}Pb	63.9	753	SPP	11.3	58.8	5.19	0.65	14.3
^{12}C+^{208}Pb	61.4	429	SPP	11.5	57.7	4.70	0.79	8.5
^{17}Ne+^{208}Pb	125.7	1800	SPP	11.5	95.9	5.02	5.95	67.9
^{12}N+^{197}Au	66.0	1269	SPP	11.2	66.2	5.04	-0.04	26.3
			V_{00}	11.2	65.6	4.90	0.08	27.7
			Pol.	11.2	64.1	4.88	0.39	27.9
^{14}N+^{197}Au	85.9	822	SPP	11.4	65.1	4.63	4.48	23.3

systems because the parabolic fitted barrier tends to be more transparent than the actual barrier and, consequently, underestimates fusion cross sections. Moreover, contributions from non negligible angular momenta are not explicitly considered. Nevertheless, $\sigma_{\rm UFF}$ can be reasoned as a lower limit for $\sigma_{\rm Red}$ due to fusion.

The Table II shows the reaction cross section σ_R for some systems at energies close to the Coulomb barrier available in the literature. The σ_R for the ^{12}N+^{197}Au system is large compared to tightly bound systems, such as ^{14}N+^{197}Au (σ_R = 822 mb) and ^{12}C+^{208}Pb (σ_R = 429 mb) [17], and comparable to the ^{8}B+^{208}Pb (σ_R = 1112 mb). In the latter system, break-up is an important channel that contributes to σ_R due to the low proton binding energy in the ^{8}B nucleus (S_p = 0.138 MeV). In this sense, it is also expected that break-up channel could be important in the ^{12}N+^{197}Au system as well, since the proton separation energy in ^{12}N is also small (S_p = 0.600 MeV). This expectation is supported by large inclusive break-up cross sections for the ^{12}N+^{208}Pb system at higher energies ($E_{\rm lab}$ = 343 MeV) [24].

Fig. 4 shows the $\sigma_{\rm Red,1}$ for several light projectiles on ^{197}Au and ^{208}Pb targets. The $\sigma_{\rm Red,1}$ for stable projectiles (^{6,7}Li and ^{12}C) lies close to the UFF curve, which means that

fusion is the main reaction channel to $\sigma_{\rm Red}$. The reduced cross sections for systems with neutron/proton-rich unstable projectiles, such as ^{6}He and ^{7}Be, are above those for stable projectiles. In these projectiles, break-up is another important channel and the $\sigma_{\rm Red,1}$ values are roughly twice that for stable projectiles. Although the separation energy of ^{10}Be is high (S_n=6.812 MeV), the cross sections are quite close to the UFF curve, which requires further investigation. In this plot, we observe astonishingly high $\sigma_{\rm Red}$ values for the reduced cross section for ^{8}B and ^{12}N, which are well above the UFF curve for the other neutron-rich projectiles. It is not clear whether break-up or limitations of the adopted reduction method is responsible for this apparent huge enhancement of $\sigma_{\rm Red}$.

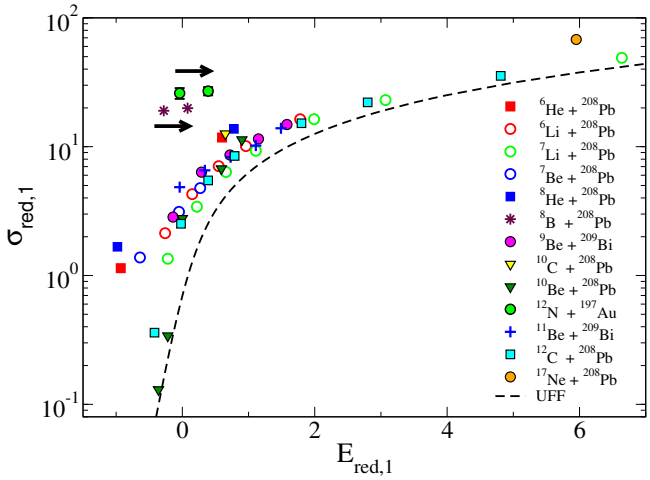

FIG. 4: Reduced total reaction cross section as a function of reduced energy for some selected system (on heavy target), using the reduction method described in the text. The dashed line curve is the Universal Fusion Function (UFF), representing the fusion limit. Black arrows indicate the points for the ^{12}N+^{197}Au and ^{8}B+^{208}Pb systems when different potentials are used to determine the barrier parameters. See text for discussions.

A shortcoming of the reaction function method is that it is heavily dependent on the Coulomb barrier parameters, which in turn may depend on the particular nuclear optical potential. It is usual to consider double folding potentials and, therefore, in this work we adopt the São Paulo potential (SPP) [25] without a centrifugal term ($\ell = 0$). This is a double-folding potential that uses a two-parameter Fermi shape for the density distributions of the projectile and target nuclei. Parameters were determined from a systematic analysis and therefore do not account for cluster configurations of either the projectile or the target nuclei. In Table II we list the parameters R_b, V_b and $\hbar\omega$ adjusted to the Coulomb barrier as

defined by the SPP for some systems.

It has been pointed out that the reaction function method depends on a suitable determination of the barrier parameters [19]. There is also the possibility that the cluster configurations of the projectile affect the Coulomb barrier. Considering the cluster configuration for ^{12}N, we can plot three situations regarding the interaction between the weakly bound proton-rich projectile and the heavy target nuclei, as shown in Fig. 5. The double folding SPP assumes standard matter densities distributions that is sketched in Fig. 5a. However, the halo structure makes the Coulomb barrier lower than the one given by the SPP calculated directly for the projectile-target system. Within the framework of the continuum discretized coupled-channel (CDCC), we can define the V_{00} potential as:

$$V_{00}(r) = \int d^3\vec{r} |\psi_0(\vec{r})|^2 \left[U_{pT}(\vec{r}_{pT}) + U_{cT}(\vec{r}_{cT})\right], \tag{3}$$

where $\psi_0(\vec{r})$ is the ground-state wave function of the halo nucleus, $U_{pT}(\vec{r}_{pT})$ and $U_{cT}(\vec{r}_{cT})$ represent the proton-target and core-target interactions, respectively. This situation is represented in Fig. 5b.

The dynamic polarization of the proton-rich projectile is another feature that must be considered. In this process, Coulomb repulsion between colliding particles pushes the valence proton away from its nuclear core. This corresponds to a displacement of the valence proton that produces an effective attenuation of the Coulomb barrier of the system. The extreme picture of polarization is represented in Fig. 5c, in which the valence proton is behind its nuclear core. In this scheme, we approximate the interaction between the projectile and the target ($V_{\text{pol.}}$) by:

$$V_{\text{pol.}}(r) = U_{cT}(r_{cT}) + U_{pT}(r_{cT} + r_{\text{halo}}). \tag{4}$$

This produces a lower barrier compared to the previous ones.

A comparison between the Coulomb barriers produced by the V_{SPP}, V_{00} and $V_{\text{pol.}}$ interactions for the ^{12}N+^{197}Au system is shown in Fig. 6. The V_b, obtained from an inverted parabola fitted to the barrier, is higher for the V_{SPP} (66.2 MeV) and lower for the $V_{\text{pol.}}$ (64.1 MeV). The V_{00} height is only 0.6 MeV below the V_{SPP} one. The R_b and $\hbar\omega$ among these nuclear potentials do not change significantly (less than 3%). These values are reported in Table II for the ^{8}B+^{208}Pb and ^{12}N+^{197}Au systems. The reduced quantities based on these barriers can be calculated. We plot the reduced total reaction cross section in Fig. 4 as green circles (for ^{12}N) and purple asterisks (for ^{8}B). The lower V_b displaces the

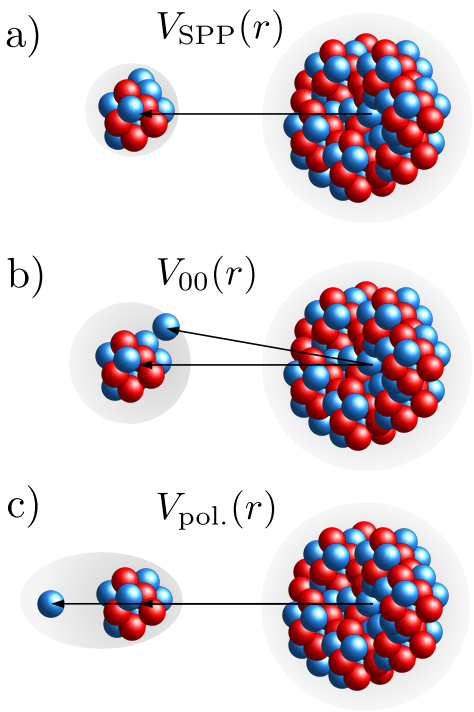

FIG. 5: Illustrative representation of different nuclear potentials between the colliding partners adopted to define the Coulomb barrier: (a) represents the double folding SPP, with no cluster structure for the projectile; (b) represents the V_{00} potential, in which the cluster configuration in the ground state of the projectile is taken into account; (c) illustrate the extreme case of dynamic polarization, in which the proton valence particle sets behind its nuclear core.

data points toward positive E_{Red} values, without significant changes in σ_{Red} (also indicated by black arrows in Fig. 4). Data points are still above the UFF curve (fusion) in both systems; however, this simple approach suggests that a larger σ_R is characteristic in weakly bound proton-rich projectiles, which results from the dynamic polarization and reduction of the Coulomb barrier. Dynamic polarization also appears in reactions with neutron-rich nuclei, but the subsequent attenuation in V_b seems to be smaller because the electric charge of the projectile is in the nuclear core.

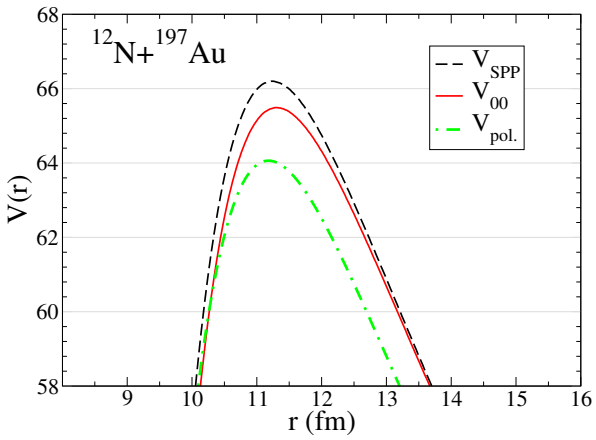

FIG. 6: Detail of the Coulomb barrier for the ^{12}N+^{197}Au system using the double folding São Paulo potential (SPP) and the V_{00} potential, obtained from a folding with the ground-state wave function for the $p-^{11}$C configuration. See text for details.

2. The simplified traditional method

This method avoids using the barrier parameters required in the previous methods, which make it model dependent. Transformations depend on geometrical parameters instead and are based on the approximate relations to R_b and V_b:

$$R_b \propto \left[A_p^{1/3} + A_t^{1/3}\right], \qquad V_b \propto \frac{Z_p Z_t}{A_p^{1/3} + A_t^{1/3}}, \tag{5}$$

where A_i and Z_i are the atomic mass and atomic number, respectively, for projectile nuclei ($i = p$) and target ($i = t$) nuclei. The reduced variables are:

$$E_{\rm Red,2} = \frac{Z_p Z_t}{A_p^{1/3} + A_t^{1/3}} E_{\rm c.m.} \qquad \sigma_{\rm Red,2} = \frac{\sigma_R}{A_p^{1/3} + A_t^{1/3}}. \tag{6}$$

This method depends on the charges and masses of the nuclei and, therefore, is model independent. However, there is no physical meaning attached to the $E_{\rm Red,2}$ and $\sigma_{\rm Red,2}$ values. In the previous method, for example, $E_{\rm Red,1} = 0$ corresponds to the barrier height of the systems and $\sigma_{\rm UFF}$ sets a lower limit to $\sigma_{\rm Red,1}$.

In Fig. 7 we show a comparison between some selected systems using the simplified traditional method. The ^{12}N+^{197}Au and ^{8}B+^{208}Pb now lies along the same trend as the ^{6,8}He+^{208}Pb systems. From this point of view, our estimate for the total reaction cross section for the ^{12}N+^{197}Au system is connected to the spatial extension of the projectile nuclei that can be considered as static (halo structure) or dynamic (polarization) effects.

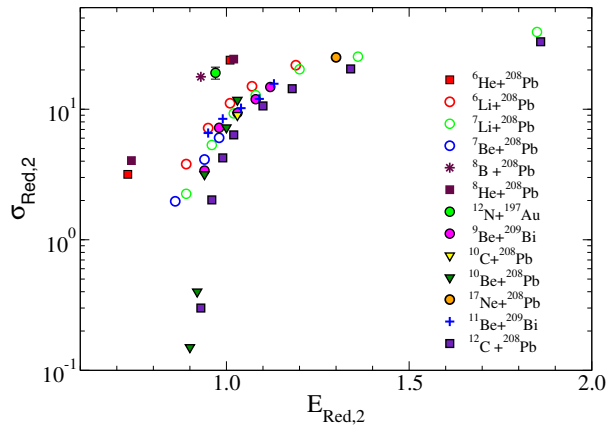

FIG. 7: Reduced total reaction cross section as a function of reduced energy for some selected system (on heavy target), using the simplified traditional method. See text for discussions.

Detailed study on this topic is beyond the scope of this work, and further data for proton-rich is needed. However, we can conclude that the total reaction cross sections for both ^{8}B and ^{12}N are similar.

C. Continuum discretized coupled-channels calculations

In this section, we discuss the contribution of the elastic breakup in the total reaction cross section based on the three-body continuum discretized coupled channels (CDCC). Calculations were performed using the computer code FRESCO [26]. The internal structure of the target is ignored, while the weakly bound nature of the ^{12}N projectile is modeled as a ^{11}C+p system. In the ground state, the valence proton moves around the core in the $1p_{1/2}$ orbital.

The intrinsic Hamiltonian necessary to create the projectile ground state contains a nuclear interaction with parameters chosen to reproduce the halo radius ($r_{\rm halo}$) for the ^{11}C-p model. The $r_{\rm halo}$ is related to the root mean square radius ($r_{\rm rms}$) of the nuclei ^{12}N and ^{11}C as follows:

$$r^2_{\rm halo} = [12 \times r^2_{\rm rms}(^{12}{\rm N})] - [11 \times r^2_{\rm rms}(^{11}{\rm C})]. \quad (7)$$

The above mentioned equation neglects the spatial extent of the ^{11}C and proton. We have found two different $r_{\rm rms}$ values reported in the literature [27, 28]. Based on these values, we obtain value for $r_{\rm halo}$ of 4.18 and 4.47 fm.

This nucleus has no excited bound state, and the remaining projectile states included in the model space are in the continuum. These continuum states are square-integrable wave functions obtained by taking the energy average of ^{11}C + p scattering states within a given energy range. They are then labeled by the midpoint of the energy interval and by its angular momentum. The continuum was built with a fixed width equal to 2 fm^{-1} in the momentum space, and orbital angular momenta up to $\ell = 2\hbar$ were considered. According to Ref. [29], the ^{12}N nuclei presents some resonant states from which the $J^{\pi} = 2^{-}$ and $J^{\pi} = 1^{-}$ are the most intense ones. These resonances were constructed using a thinner mesh around their corresponding excitation energy (E = 0.6 and 1.2 MeV, respectively) and using nuclear interactions with a parameter slightly different from the one used to create the ground state.

The CDCC approach consists of solving the coupled equation with p-target ($U_{\mathrm{p,T}}$) and core-target ($U_{^{11}\mathrm{C,T}}$) interactions. These are the optical potentials responsible for the elastic scattering of the valence particle (p) and the core (^{11}C) with the target (^{197}Au) that contain both the Coulomb and nuclear components. The complex nuclear potential considered in this work was the Koning-Delaroche [30] for p-target interaction and Akyüs-Winther [31] for core-target interaction. To solve the set of coupled equations, the matrix elements $V_{\alpha,\alpha'}(R)$ were expanded to multipoles up to $\lambda = 3$ and the equations were solved numerically. We considered radial distances up to $R = 150$ fm and angular momenta up to $J = 500\hbar$.

Fig. 8 shows the experimental elastic angular distribution compared to calculations. The one-channel calculation (dashed magenta curve) takes into account only the projectile ground state, without couplings with the continuum and assuming $r_{\mathrm{halo}} = 4.17$ fm. These couplings (with the continuum) are considered in the CDCC calculations (solid black curve), causing a small suppression of the cross section at forward angles ($\theta < 90^{\circ}$) and enhancement at backward angles.

To investigate the effect of the parameter r_{halo}, adopted to construct the intrinsic states in the nucleus ^{12}N, we performed two additional CDCC calculations assuming $r_{\mathrm{halo}} = 4.47$ and (a hypothetical) r_{halo}=5.00 fm. The results of these calculations are shown as dot-dashed blue and dotted orange curves, respectively, in Fig. 8. The agreement with the experimental data is limited and the r_{halo} changes a little the elastic cross section at the grazing angles. Other calculations (not shown) using different optical potentials for the core-target interaction and neglecting resonant states in ^{12}N deteriorate the agreement with the experimental data. In this work we have not performed four-body CDCC, in which the

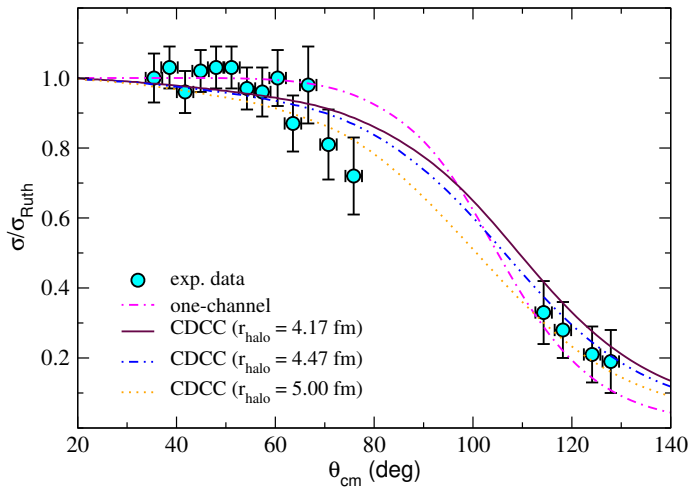

FIG. 8: Elastic scattering angular distribution for the ^{12}N+^{197}Au. The solid line corresponds to the full CDCC calculation whereas the dot-dashed line is the calculation with no coupling to the unbound states.

TABLE III: : Reaction, absorption (abs.) and elastic breakup (EBU) cross sections as obtained from the one-channel and the CDCC calculations.

calculation	σ_R (mb)	$\sigma_{\rm abs.}$ (mb)	$\sigma_{\rm EBU}$ (mb)
one-channel	676	676	–
CDCC	1297	605	692

^{12}N is modeled as a ^{10}B+p+p system. It is unlikely that this configuration gives a significant contribution to elastic scattering because the two-proton separation energy in ^{12}N is quite high ($S_{\rm 2p} = 9.29$ MeV).

Measurements of the break-up cross sections will be important to improve our study. In Table III, we provide the reaction, absorption, and (elastic) breakup cross sections obtained in the one-channel (no coupling) and full CDCC. According to the full CDCC, the elastic break-up accounts for 54% of the reaction cross section.

IV. CONCLUSIONS

In summary, this work reports new experimental data for elastic scattering of the ^{12}N+^{197}Au system at $E_{\rm lab}$=70 MeV. The reaction cross section, as obtained from the optical model fitted to the data, is large ($\sigma_R = 1269 \pm 41$ mb). Using a reduction method to

compare the reaction cross section among many systems, we show that our obtained value is as large as the one measured for the ^{8}B+^{208}Pb in Ref. [7]. A possible interpretation for the large σ_R observed in weakly bound proton-rich projectiles is the decoupling of a valence proton from the core due to the low binding energy and the dynamic polarization effect. The ultimate effect is a reduction of the Coulomb barrier that leads to higher reaction cross sections compared to other weakly bound projectiles. A systematic analysis is needed to study in depth the dynamic polarization in proton-rich nuclei. In addition, further theoretical models are required to describe the full angular range of the present experimental data, such as the inclusion of other channel decay and/or excitation of the ^{11}C core and ^{197}Au target nuclei.

ACKNOWLEDGMENTS

This work was partially supported by the U.S. Department of Energy, Office of Science, Office of Nuclear Science under award no. DE-FG02-93ER40773. The authors also thank the following foundations for financial support: CNPq (Grants 317451/2021-9, 403390/2021-4 and 131272/2022-5), Institutos Nacionais de Ciências e Tecnologia–Fisica Nuclear e Aplicações (INCT/FNA) Proc. No. 464898/2014-5, FAPESP (processes 2019/08344-7, 2016/17612-7 and 2024/02463-2). Also, we would like to thank the operators team at the Cyclotron Institute of Texas A&M University for reliable operation of the Cyclotron during the data acquisition that generated this work.

[1] I. Tanihata, H. Hamagaki, O. Hashimoto, Y. Shida, N. Yoshikawa, K. Sugimoto, O. Yamakawa, T. Kobayashi, and N. Takahashi, Phys. Rev. Lett. **55**, 2676 (1985).

[2] Y. Ye, X. Yang, H. Sakurai, , and B. Hu, Nat. Rev. Phys. **7**, 21 (2025).

[3] N. Michel, W. Nazarewicz, J. Okołowicz, and M. Płoszajczak, Journal of Physics G: Nuclear and Particle Physics **37**, 064042 (2010).

[4] N. Keeley, N. Alamanos, K. W. Kemper, and K. Rusek, Phys. Rev. C **82**, 034606 (2010).

[5] A. Diaz-Torres and A. M. Moro, Physics Letters B **733**, 89 (2014).

[6] I. Tanihata, H. Savajols, and R. Kanungo, Progress in Particle and Nuclear Physics **68**, 215 (2013).

[7] M. Mazzocco, N. Keeley, A. Boiano, C. Boiano, M. La Commara, C. Manea, C. Parascandolo, D. Pierroutsakou, C. Signorini, E. Strano, D. Torresi, H. Yamaguchi, D. Kahl, L. Acosta, P. Di Meo, J. P. Fernandez-Garcia, T. Glodariu, J. Grebosz, A. Guglielmetti, Y. Hirayama, N. Imai, H. Ishiyama, N. Iwasa, S. C. Jeong, H. M. Jia, Y. H. Kim, S. Kimura, S. Kubono, G. La Rana, C. J. Lin, P. Lotti, G. Marquínez-Durán, I. Martel, H. Miyatake, M. Mukai, T. Nakao, M. Nicoletto, A. Pakou, K. Rusek, Y. Sakaguchi, A. M. Sánchez-Benítez, T. Sava, O. Sgouros, V. Soukeras, F. Soramel, E. Stiliaris, L. Stroe, T. Teranishi, N. Toniolo, Y. Wakabayashi, Y. X. Watanabe, L. Yang, Y. Y. Yang, and H. Q. Zhang, Phys. Rev. C **100**, 024602 (2019).

[8] R. Spartà, A. Di Pietro, P. Figuera, O. Tengblad, A. Moro, I. Martel, J. Fernández-García, J. Lei, L. Acosta, M. Borge, G. Bruni, J. Cederkäll, T. Davinson, J. Ovejas, L. Fraile, D. Galaviz, J. Halkjaer Jensen, B. Jonson, M. La Cognata, A. Perea, A. Sánchez-Benítez, N. Soić, and S. Viñals, Physics Letters B **820**, 136477 (2021).

[9] L. Yang, C. J. Lin, H. Yamaguchi, A. M. Moro, N. R. Ma, D. X. Wang, K. J. Cook, M. Mazzocco, P. W. Wen, S. Hayakawa, J. S. Wang, Y. Y. Yang, G. L. Zhang, Z. Huang, A. Inoue, H. M. Jia, D. Kahl, A. Kim, M. S. Kwag, M. L. Commara, G. M. Gu, S. Okamoto, C. Parascandolo, D. Pierroutsakou, H. Shimizu, H. H. Sun, M. L. Wang, F. Yang, and F. P. Zhong, Nature Communications **13**, 7193 (2023).

[10] R. Linares, M. Sinha, E. N. Cardozo, V. Guimarães, G. V. Rogachev, J. Hooker, E. Koshchiy, T. Ahn, C. Hunt, H. Jayatissa, S. Upadhyayula, B. Roeder, A. Saastomoinen, J. Lubian, M. Rodríguez-Gallardo, J. Casal, K. C. C. Pires, M. Assunção, Y. Penionzhkevich, and S. Lukyanov, Physical Review C **103**, 10.1103/physrevc.103.044613 (2021).

[11] J. Ovejas, I. Martel, D. Dell'Aquila, L. Acosta, J. Aguado, G. de Angelis, M. Borge, J. Briz, A. Chbihi, G. Colucci, C. Díaz-Martín, P. Figuera, D. Galaviz, C. García-Ramos, J. Gómez-Galán, C. Gonzales, N. Goyal, N. Keeley, K. Kemper, T. Kurtukian Nieto, D. Malenica, M. Mazzocco, D. Nurkić, A. Orduz, A. Ortiz, L. Palada, C. Parascandolo, A. Di Pietro, A. Rodriguez, K. Rusek, F. Salguero, A. Sánchez-Benítez, M. Sánchez-Raya, J. Sánchez-Segovia, N. Soić, F. Soramel, M. Stanoiu, O. Tengblad, N. Vukman, and M. Xarepe, Physics Letters B **843**, 138007 (2023).

[12] E. Pollacco, G. Grinyer, F. Abu-Nimeh, T. Ahn, S. Anvar, A. Arokiaraj, Y. Ayyad, H. Baba, M. Babo, P. Baron, D. Bazin, S. Beceiro-Novo, C. Belkhiria, M. Blaizot, B. Blank, J. Bradt,

G. Cardella, L. Carpenter, S. Ceruti, E. De Filippo, E. Delagnes, S. De Luca, H. De Witte, F. Druillole, B. Duclos, F. Favela, A. Fritsch, J. Giovinazzo, C. Gueye, T. Isobe, P. Hellmuth, C. Huss, B. Lachacinski, A. Laffoley, G. Lebertre, L. Legeard, W. Lynch, T. Marchi, L. Martina, C. Maugeais, W. Mittig, L. Nalpas, E. Pagano, J. Pancin, O. Poleshchuk, J. Pedroza, J. Pibernat, S. Primault, R. Raabe, B. Raine, A. Rebii, M. Renaud, T. Roger, P. Roussel-Chomaz, P. Russotto, G. Saccà, F. Saillant, P. Sizun, D. Suzuki, J. Swartz, A. Tizon, A. Trifiró, N. Usher, G. Wittwer, and J. Yang, Nuclear Instruments and Methods in Physics Research Section A: Accelerators, Spectrometers, Detectors and Associated Equipment **887**, 81 (2018).

[13] E. Koshchiy, G. Rogachev, E. Pollacco, S. Ahn, E. Uberseder, J. Hooker, J. Bishop, E. Aboud, M. Barbui, V. Goldberg, C. Hunt, H. Jayatissa, C. Magana, R. O'Dwyer, B. Roeder, A. Saastamoinen, and S. Upadhyayula, Nuclear Instruments and Methods in Physics Research Section A: Accelerators, Spectrometers, Detectors and Associated Equipment **957**, 163398 (2020).

[14] S. Agostinelli *et al.*, Nuclear Instruments and Methods in Physics Research Section A: Accelerators, Spectrometers, Detectors and Associated Equipment **506**, 250 (2003).

[15] L. E. Tamayose, J. C. Zamora, G. F. Fortino, and D. Flechas, Brazilian Journal of Physics **52**, 89 (2022).

[16] G. Baur, C. Bertulani, and D. Kalassa, Nuclear Physics A **550**, 527 (1992).

[17] S. Santra, P. Singh, S. Kailas, A. Chatterjee, A. Shrivastava, and K. Mahata, Phys. Rev. C **64**, 024602 (2001).

[18] G. Balster, P. Crouzen, P. Goldhoorn, R. Siemssen, and H. Wilschut, Nuclear Physics A **468**, 93 (1987).

[19] L. F. Canto, D. R. M. Junior, P. R. S. Gomes, and J. Lubian, Phys. Rev. C **92**, 014626 (2015).

[20] J. Shorto, P. Gomes, J. Lubian, L. Canto, S. Mukherjee, and L. Chamon, Physics Letters B **678**, 77 (2009).

[21] L. Canto, P. Gomes, J. Lubian, L. Chamon, and E. Crema, Nuclear Physics A **821**, 51 (2009).

[22] C. Y. Wong, Phys. Rev. Lett. **31**, 766 (1973).

[23] L. F. Canto, P. R. S. Gomes, J. Lubian, L. C. Chamon, and E. Crema, Journal of Physics G: Nuclear and Particle Physics **36**, 015109 (2008).

[24] K. Wang, Y. Y. Yang, J. Lei, A. M. Moro, V. Guimarães, J. G. Li, F. F. Duan, Z. Y. Sun, G. Yang, D. Y. Pang, S. W. Xu, J. B. Ma, P. Ma, Z. Bai, Q. Liu, J. L. Lou, H. J. Ong, B. F. Lv, S. Guo, M. K. Raju, X. H. Wang, R. H. Li, X. X. Xu, Z. Z. Ren, Y. H. Zhang, X. H.

Zhou, Z. G. Hu, and H. S. Xu (RIBLL Collaboration), Phys. Rev. C **109**, 014624 (2024).

[25] L. C. Chamon, B. V. Carlson, L. R. Gasques, D. Pereira, C. De Conti, M. A. G. Alvarez, M. S. Hussein, M. A. Cândido Ribeiro, E. S. Rossi, and C. P. Silva, Phys. Rev. C **66**, 014610 (2002).

[26] I. J. Thompson, Computer Physics Reports **7**, 167 (1988).

[27] A. Ozawa, I. Tanihata, T. Kobayashi, D. Hirata, O. Yamakawa, K. Omata, N. Takahashi, T. Shimoda, K. Sugimoto, D. Olson, W. Christie, and H. Wieman, Nuclear Physics A **583**, 807 (1995), nucleus-Nucleus Collisions.

[28] L. Jia-Xing, L. Ping-Ping, W. Jian-Song, H. Zheng-Guo, M. Rui-Shi, L. Chen, C. Ruo-Fu, S. Zhi-Yu, X. Hu-Shan, X. Guo-Qing, and G. Zhong-Yan, Chinese Physics Letters **27**, 032501 (2010).

[29] T. Teranishi, S. Kubono, S. Shimoura, M. Notani, Y. Yanagisawa, S. Michimasa, K. Ue, H. Iwasaki, M. Kurokawa, Y. Satou, T. Morikawa, A. Saito, H. Baba, J. Lee, C. Lee, Z. Fülöp, and S. Kato, Physics Letters B **556**, 27 (2003).

[30] A. Koning and J. Delaroche, Nuclear Physics A **713**, 231 (2003).

[31] R. Broglia and A. Winther, *Heavy Ion Reactions: Lecture Notes*, Frontiers in physics No. v. 1 (Benjamin/Cummings, 1981).

[32] T. Teranishi, S. Kubono, S. Shimoura, M. Notani, Y. Yanagisawa, S. Michimasa, K. Ue, H. Iwasaki, M. Kurokawa, Y. Satou, T. Morikawa, A. Saito, H. Baba, J. Lee, C. Lee, Z. Fülöp, and S. Kato, Physics Letters B **556**, 27 (2003).

[33] M. Wiescher, J. Gorres, S. Graff, L. Buchmann, and F.-K. Thielemann, The Astrophysical Journal **343**, 352 (1989).

[34] V. Guimarães, E. N. Cardozo, V. B. Scarduelli, J. Lubian, J. J. Kolata, P. D. O'Malley, D. W. Bardayan, E. F. Aguilera, E. Martinez-Quiroz, D. Lizcano, A. Garcia-Flores, M. Febbraro, C. C. Lawrence, J. Riggins, R. O. Torres-Isea, P. N. de Faria, D. S. Monteiro, E. S. Rossi, and N. N. Deshmukh, Phys. Rev. C **100**, 034603 (2019).

[35] G. Korolev, A. Dobrovolsky, A. Inglessi, G. Alkhazov, P. Egelhof, A. Estradé, I. Dillmann, F. Farinon, H. Geissel, S. Ilieva, Y. Ke, A. Khanzadeev, O. Kiselev, J. Kurcewicz, X. Le, Y. Litvinov, G. Petrov, A. Prochazka, C. Scheidenberger, L. Sergeev, H. Simon, M. Takechi, S. Tang, V. Volkov, A. Vorobyov, H. Weick, and V. Yatsoura, Physics Letters B **780**, 200 (2018).

[36] Y. Kucuk and E. Aciksoz, European Physical Journal A **52**, 98 (2016).

[37] E. F. Aguilera, E. Martinez-Quiroz, D. Lizcano, A. Gómez-Camacho, J. J. Kolata, L. O. Lamm, V. Guimarães, R. Lichtenthäler, O. Camargo, F. D. Becchetti, H. Jiang, P. A. DeYoung, P. J. Mears, and T. L. Belyaeva, Phys. Rev. C **79**, 021601 (2009).

[38] J. Liang, J. Beene, A. Caraley, H. Esbensen, A. Galindo-Uribarri, C. Gross, P. Mueller, K. Schmitt, D. Shapira, D. Stracener, and R. Varner, Physics Letters B **681**, 22 (2009).

[39] J. Rangel, J. Lubian, L. F. Canto, and P. R. S. Gomes, Phys. Rev. C **93**, 054610 (2016).

[40] M. Romoli, E. Vardaci, M. Di Pietro, A. De Francesco, A. De Rosa, G. Inglima, M. La Commara, B. Martin, D. Pierroutsakou, M. Sandoli, M. Mazzocco, T. Glodariu, P. Scopel, C. Signorini, R. Bonetti, A. Guglielmetti, F. Soramel, L. Stroe, J. Greene, A. Heinz, D. Henderson, C. L. Jiang, E. F. Moore, R. C. Pardo, K. E. Rehm, A. Wuosmaa, and J. F. Liang, Phys. Rev. C **69**, 064614 (2004).

[41] M. Kamimura, M. Yahiro, Y. Iseri, Y. Sakuragi, H. Kameyama, and M. Kawai, Progress of Theoretical Physics Supplement **89**, 1 (1986), https://academic.oup.com/ptps/article-pdf/doi/10.1143/PTPS.89.1/5376379/89-1.pdf.

[42] N. Austern, Y. Iseri, M. Kamimura, M. Kawai, G. Rawitscher, and M. Yahiro, Physics Reports **154**, 125 (1987).